Understanding the bactericidal mechanism of Cu(OH)2 nanorods in water through Mg-substitution: high production of toxic hydroxyl radicals by non-soluble particles

Batiste Clavier, Téo Baptiste, Antonii Zhadan, Amandine Guiet, Fabien Boucher, Vlasta Brezová, Christine Roques, Gwenaël Corbel

Understanding the bactericidal mechanism of $Cu(OH)_2$ nanorods in water through Mg-substitution: high production of toxic hydroxyl radicals by non-soluble particles

Batiste Clavier [1], Téo Baptiste [1], Antonii Zhadan [1], Amandine Guiet [1], Fabien Boucher [2], Vlasta Brezová [3], Christine Roques [4,5] and Gwenaël Corbel [1]*

[1] *Institut des Molécules et Matériaux du Mans (IMMM), UMR-6283 CNRS, Le Mans Université, Avenue Olivier Messiaen, 72085 Le Mans Cedex 9, France*
[2] *Institut Universitaire de Technologie du Mans, Le Mans Université, Avenue Olivier Messiaen, 72085 Le Mans Cedex 9, France*
[3] *Institute of Physical Chemistry and Chemical Physics, Faculty of Chemical and Food Technology, Slovak University of Technology in Bratislava, Radlinského 9, SK-812 37 Bratislava, Slovakia*
[4] *Laboratoire de Génie Chimique, UMR-5503 CNRS, Faculté de Pharmacie, Université Paul Sabatier - Toulouse III, 35, chemin des maraîchers, 31062 Toulouse Cedex 4, France*
[5] *Centre Hospitalier Universitaire (CHU) de Toulouse, Institut Fédératif de Biologie (IFB), Laboratoire de Bactériologie et Hygiène, 330 Avenue de Grande Bretagne, 31059 Toulouse Cedex 9, France*
* *E-mail: gwenael.corbel@univ-lemans.fr ; Fax: +33 (0)2 43 83 35 06 ; Tel: +33 (0)2 43 83 26 48 ; ORCID : 0000-0003-2605-7702*

Abstract

To date, there is still a lack of definite knowledge regarding the toxicity of $Cu(OH)_2$ nanoparticles towards bacteria. This study was aimed at shedding light on the role played by released cupric ions in the toxicity of nanoparticles. To address this issue, the bactericidal activity of $Cu(OH)_2$ was at first evaluated in sterile water, a medium in which particles are not soluble. In parallel, an isovalent substitution of cupric ions by Mg^{2+} was attempted in the crystal structure of $Cu(OH)_2$ nanoparticles to increase their solubility and determine the impact on the bactericidal activity. For the first time, mixed $Cu_{1-x}Mg_x(OH)_2$ nanorods ($x \leq 0.1$) of about 15 nm in diameter and a few hundred nanometers in length were successfully prepared by a simple co-precipitation at room temperature in mixed alkaline ($NaOH/Na_2CO_3$) medium. For *E. coli*, 100% reduction of one million CFU per mL (6 log_{10}) occurs after only 180 min on contact with both $Cu(OH)_2$ and $Cu_{0.9}Mg_{0.1}(OH)_2$ nanorods. The entire initial inoculum of *S. aureus* is also killed by $Cu(OH)_2$ after 180 min (100% or 6 log_{10} reduction), while 0.01% of these bacteria stay alive on contact with $Cu_{0.9}Mg_{0.1}(OH)_2$ (99.99% or 4 log_{10} reduction). The bactericidal performances of $Cu(OH)_2$ and the magnesium-substituted counterparts (*i.e.* $Cu_{1-x}Mg_x(OH)_2$) are not linked to cupric ions they release in water since their mass concentrations after 180 min are much lower than minimal concentrations inhibiting the growth of *E. coli* and *S. aureus*. Finally, an EPR spin trapping study reveals how these nanorods kill bacteria in water: only the presence of hydrogen peroxide, a by-product of the normal metabolism of oxygen in aerobic bacteria, allows the $Cu(OH)_2$ and its magnesium-substituted counterparts to produce a lethal amount of free radicals, the majority of which are the highly toxic $HO^{\bullet}$.

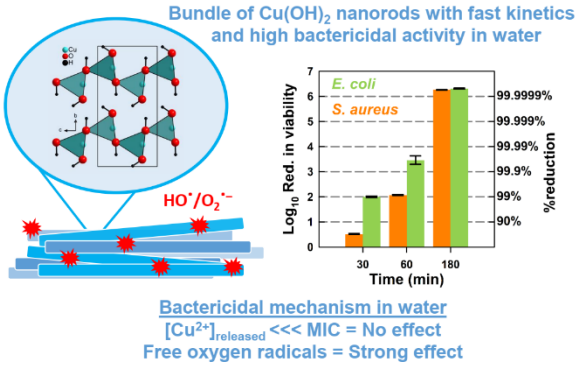

Electronic supplementary information (ESI) available: 1- Experimental details. 2- Thermal decomposition of $Cu_{0.95}Mg_{0.05}(OH)_2$ and $Cu_{0.85}Mg_{0.15}(OH)_2$ samples monitored by ThermoGravimetric (TG) - Mass Spectrometric (MS) evolved gas analyses. 3- Crystallographic data of $Cu_{1-x}Mg_x(OH)_2$ samples. 4- Bactericidal activity of bi-phasic $Cu_{0.85}Mg_{0.15}(OH)_2$ and $Cu_{0.80}Mg_{0.20}(OH)_2$ samples. 5- EPR spectra of the aerated water suspensions of $Cu(OH)_2$ and $Cu_{0.90}Mg_{0.10}(OH)_2$ nanorods in the presence of DMPO spin trapping agent.

1-Introduction

Large-scale production of fresh produce requires a lot of irrigation during the growing season and the agricultural water withdrawal accounts for 44% of total freshwater use in OECD countries (Organisation for Economic Co-operation and Development), and over 90% in the least developed countries.[1] In agriculture, irrigation waters are directly pumped in nearby streams, canals, ponds, wells and dams. Faecal contamination of freshwater from wildlife, waterfowl, or agricultural animals results in a high prevalence of *E. coli* in sediments.[2] In the absence of turbulence, sediments contribute very little to the bacterial load of surface waters. When freshwater is pumped or released from reservoirs, a resuspension of sediment occurs[2] and *E. coli* together with other enteric bacteria can then contaminate fruits and vegetables sprinkled with this water in fields.[3] Such a situation can occur because the microbial load of agricultural surface waters is not monitored in comparison to drinking and recreational waters. By way of example, seven

countries in Europe reported in June 2011 an ongoing *E. coli* outbreak associated with the consumption of fresh sprouted seeds imported from Egypt.[4] At the end of 2015, a threshold concentration of *E. coli* of 410 Colony Forming Units (CFU) in a 100 mL water sample was defined as the quality requirements for agricultural water by the U.S. Food and Drug Administration.[5] In order to meet this water quality standard, disinfection or other processes able to reduce microbial loads in agricultural water may be necessary.

Greywater (GW) is defined as household wastewater from bathroom sinks, bath, showers and washing machines, only.[6] Humans are a natural reservoir of *S. aureus* which colonized nares, axillae, vagina, pharynx or skin.[7] Since wash water is a major component of GW, this peripheral opportunistic pathogen may be present in addition to enteric bacteria as *E. coli*, which is rarely the case for surface water sources.[8] The use of GW has been considered for on-site irrigation in areas where water reserves are scarce.[9,10] But the recycling of GW for irrigation also poses a potential risk of infections for humans.[11,12] This is especially true when opportunistic pathogens, as *S. aureus* and *P. aeruginosa*, can survive to the biological treatment of GW for 72 h by using a recycling vertical flow constructed wetland (RVFCW)[13] and then proliferate. One way to efficiently disinfect GW could be to add a non-soluble antibacterial agent to the filter medium of the RVFCW. The advantage of this method over treating water with molecular dichlorine is that it does not produce carcinogenic disinfection by-products such as trihalomethanes (THMs)[14,15] and is less expensive than treating water with ozone. Karkhanechi *et al.*[16] improved the antibiofouling properties of reverse osmosis membranes used in water treatment processes by depositing micron-sized aggregates of cupric hydroxide particles on them. In this study, the antibiofouling properties were only evaluated against *E. coli* in the mixed Nutrient Broth (NB)–Phosphate-Buffered Saline (PBS) medium rather than in water. For an initial concentration in *E. coli* of $\approx 1\text{–}5 \times 10^5$ CFU mL^{-1} in this medium, the reported reductions in cell viability remain far below the minimum value of 99.99–99.999% (4–5 $\log_{10}$) required to meet U.S. Food and Drug Administration standards[5] even after a contact time with $Cu(OH)_2$ as long as 8 h. This moderate bactericidal activity could be due to the micrometric size of the $Cu(OH)_2$ aggregates and could be considerably improved by reducing the size of particles/aggregates to about a hundred nanometers. Karkhanechi *et al.*[16] claim that the toxicity of $Cu(OH)_2$ particles arises from the release of cupric ions into the medium although no quantification has been carried out such as by atomic emission spectroscopy (AES).

As shown by Li *et al.* for ZnO,[17] the medium components such as chloride and phosphate anions in PBS affect the toxicity of particles because these anions change the concentration of Zn^{2+} ions released from particles. A dissolution of CuO in PBS is reported by Hans *et al.*[18] Gunawan *et al.*[19] showed that the free amino acids in Luria Bertani Broth (LBB) culture medium promote the dissolution of CuO nanoparticles. However, no lysis of *E. coli* cell is observed because peptides present in the LBB medium form no toxic complexes with cupric ions thus released from CuO, which considerably reduces the amount and cytotoxic effect of free Cu^{2+} on bacteria. A similar situation certainly occurs in Karkhanechi *et al.*[16] because the NB culture medium, containing amino acids and peptides, is diluted in PBS. To determine how $Cu(OH)_2$ particles can interact with bacteria, sterile water is the medium of choice for simplifying the system to be studied. The minimal inhibitory concentrations (MIC) of free cupric ions for *E. coli* and *S. aureus* are 25 mg L^{-1} and 12.5 mg L^{-1}, respectively.[20] It is well known that free cupric ions can catalyse the generation of ROS from aqueous H_2O_2 through a Fenton-like redox cycling between Cu^{2+} and Cu^{+}/Cu^{3+} ions.[21,22] To have a bactericidal effect against *E. coli* through the ROS they produce, the concentration of free cupric ions must be equal to or greater than the MIC. In pure water, the solubility product constant of $Cu(OH)_2$ [23] is very low ($K_{sp} = 2.2 \times 10^{-20}$) and the concentration in released cupric ions cannot theoretically exceed ≈ 11.2 µg L^{-1} which is far below the MIC. Theoretically, the bactericidal activity of $Cu(OH)_2$ nanoparticles in water should therefore be very low or insignificant if released cupric ions are only responsible for their toxicity, as claimed by Karkhanechi *et al.*[16] By taking this reasoning further, $Mg(OH)_2$ is more soluble in water than its copper counterpart (solubility product constant $K_{sp} = 5.61 \times 10^{-12}$ in water[24] with a concentration in solvated Mg^{2+} of ≈ 6.53 mg L^{-1}). Thereby, a mixed $Cu_{1-x}Mg_x(OH)_2$ hydroxide resulting from the partial substitution of copper by magnesium would have a greater solubility in water and therefore a higher bactericidal activity than pure $Cu(OH)_2$ because of the increasing amount of cupric ions it would release. Comparing the bactericidal activity of pure and Mg-substituted $Cu(OH)_2$ in water is therefore a way of checking whether their dissolution alone makes them toxic or not. As simple as it sounds, no isovalent substitution of cupric ions in the layered structure of $Cu(OH)_2$ has been reported in the literature, whether with Mg^{2+} or other divalent 3d metal ions. The present study shows that such mixed hydroxides $Cu_{1-x}Mg_x(OH)_2$ do exist as single phase in a defined range of composition. The combination of X-ray diffraction, infrared spectroscopy and ThermoGravimetric (TG)-Mass Spectrometric (MS) evolved gas analyses enabled to check the phase purity as well as the chemical composition of the particle surface for each sample prepared. The morphology, size and specific surface area of particles were determined by transmission electron microscopy, X-ray diffraction, N_2 adsorption. We were finally able to assess the activity of the pure and several magnesium-substituted $Cu(OH)_2$ nanorods in water against two representative strains of pathogenic bacteria (*E. coli* CIP 53126 and *S. aureus* CIP 4.83). The expected increase in solubility caused by magnesium substitution in $Cu(OH)_2$ nanorods was also verified by atomic emission spectroscopy (AES). Against all expectations, $Cu(OH)_2$ is as active against *E. coli* as or even more active against *S. aureus* after 180 min in water than its more soluble magnesium-substituted counterparts. Finally, electron paramagnetic resonance (EPR) spin trapping technique provides the key of the toxicity of $Cu_{1-x}Mg_x(OH)_2$ nanorods in water.

2-Materials and methods

2-1) Starting materials

$MgCl_2{\cdot}6H_2O$ (Alfa Aesar, 99%), $CuCl_2$ (Acros Organics, 99%, stored in an argon-filled glove box), HNO_3 (VWR Chemicals, 68%), NaOH (Sigma-Aldrich, 98% pellets) and Na_2CO_3 (Acros Organics, 99.8%) were used as received. Commercial CuO (Alfa Aesar, 97%) contains a small amount of cuprous oxide Cu_2O. Prior to use, powder of CuO, spread over the bottom of an alumina boat, was therefore annealed at 600 °C for 12 h in a pure dioxygen gas flow (1 atm) to fully oxidize cuprous ions. Hydrogen peroxide (for analysis, 30%), 5,5-dimethyl-1-pyrroline *N*-oxide (DMPO) and 4-hydroxy-2,2,6,6-tetramethylpiperidine *N*-oxyl (TEMPOL) were purchased from Sigma-Aldrich. DMPO was distilled prior to use.

2-2) Synthesis

Nanometer-sized particles of $Cu(OH)_2$ were successfully prepared at room temperature by precipitation in mixed alkaline ($NaOH/Na_2CO_3$) medium. 50 mL of a 0.5 M copper nitrate solution is added dropwise to 150 mL of a freshly prepared mixture of 0.6 M NaOH and 0.1 M Na_2CO_3 solutions. Particular attention should be paid to the preparation of copper nitrate salt, the reasons for which are given in the Section 3.1. Precipitation occurred at room temperature instantaneously upon addition of the first drop of the copper nitrate solution, thus changing the colorless solution into a solution with blue particles in suspension. After complete delivery of the copper nitrate solution, the suspension is stirred for 30 min and then aged for 3 h without stirring. A full decantation by gravity of the blue particles took place during this ageing period. Ageing for time longer than 3 h leads to the progressive dissolution of $Cu(OH)_2$ nanoparticles in the medium and the precipitation of black CuO nanoparticles. In contrast, nanometer-sized particles of magnesium-substituted $Cu(OH)_2$ (*i.e.* $Cu_{1-x}Mg_x(OH)_2$ with $0.05 \leq x \leq 0.2$) were prepared at room temperature from a 0.5 M mixed metal chloride solution resulting from the dissolution of a stoichiometric amount of $MgCl_2{\cdot}6H_2O$ and anhydrous $CuCl_2$ in 50 mL of deionized water. The use of metal chlorides instead of nitrates is justified in Section 3.1. As previously done for precipitating nanometer-sized particles of $Cu(OH)_2$, this mixed metal chloride solution is added dropwise to 150 mL of a freshly prepared mixture of 0.6 M NaOH and 0.1 M Na_2CO_3 solutions. Here again, precipitation occurred at room temperature instantaneously upon addition of the first drop of the mixed chloride solution, thus changing the colorless solution into a solution with blue particles in suspension. After complete delivery of the mixed chloride solution, the suspension is stirred for 3 h and then aged for 15 h without stirring. A full decantation by gravity of blue particles took place during this ageing period.

For $Cu(OH)_2$ and magnesium-substituted counterparts, the absorption spectra collected on the colorless supernatant did not exhibit a broad peak in the wavelength range 500–1000 nm characteristic of d–d electronic transition of square planar $[Cu(OH)_4]^{2-}$ anion[25] or solvated divalent copper in octahedral coordination,[26] thus confirming its complete precipitation (Fig. S1 in Section S1.1, ESI†). After decantation, it is necessary to remove sodium salts (carbonate, nitrate, chloride) from the resulting precipitates. Each precipitate is then washed with deionized water and centrifuged several times at 4000 rpm for 2 min by using an Eppendorf 5804R centrifuge. After the last washing with water, the suspension of nanoparticles is drawn through a Büchner funnel by vacuum suction to recover them on a filter paper.

2-3) Characterizations and dissolution of particles

The different samples were then analyzed by X-ray powder diffraction (XRPD), transmission electron microscopy (TEM) and nitrogen sorption measurements in order to determine the phase purity, the morphology, the size and the specific surface area of particles. The monitoring of the thermal decomposition of each $Cu_{1-x}Mg_x(OH)_2$ sample was carried out by ThermoGravimetric (TG)-Mass Spectrometric (MS) evolved gas analyses and temperature-controlled XRPD. In order to check whether any dissolution of the nanometer-sized particles occurs in liquid water, the concentration in Cu^{2+} and Mg^{2+} ions released in the supernatant were measured by microwave plasma – atomic emission spectroscopy (MP-AES) analyses after 180 and 1440 min of immersion. Further experimental details about these different analyses are given in ESI† (Section S1).

2-4) Bactericidal activity experiments

The evaluation of the bactericidal activity of the hydroxide particles was carried out at 20 °C against two strains obtained from the Institute Pasteur Collection (Paris, France): *Staphylococcus aureus* CIP 4.83 and *Escherichia coli* CIP 53126. The strains were stored at −80 °C in Eugon broth (AES, Rennes, France) with 20% (v/v) glycerol (Fluka, Buchs, Switzerland). Before each experiment, preserved bacteria were grown at 36 °C under aerobic conditions on trypticase soy agar medium during 24 h (Biomérieux, Craponne, France). The second and third subcultures were used to extemporaneously prepare suspensions with a concentration in bacteria of about 2×10^8 Colony Forming Units per mL (CFU mL^{-1} calculated from the Optical Density measured at 640 nm). The as-prepared hydroxide particles were dispersed at 20 °C in sterile distilled water to obtain a suspension with an initial concentration of 1 mg mL^{-1}. For each strain, 10 mL of each particle suspension are inoculated with 100 µL of bacterial suspension, thus leading to a final concentration in bacteria of $\approx 2 \times 10^6$ CFU mL^{-1}. A bacterial suspension without particles was used as a positive control. The suspensions were then maintained at 20 °C under constant stirring on a rotary platform working at 250 shakes per min. Permanent agitation of the suspensions prevents the bacteria from adhering to the flask and ensures a good aeration of the medium (transfer of dioxygen from air to water). In addition, no sedimentation of nanoparticles occurs in our experiments with such agitation. A good distribution of bacteria and nanoparticles in the reaction volume is thus achieved. At specified times (15, 30, 60 and 180 min), 1 mL of each suspension and of the corresponding serial ten-fold dilutions were incorporated into trypticase soy agar medium poured in

flat-bottomed Petri dishes and plates were incubated at 36 °C for 48 h. The viable cell number was determined by counting the number N of bacterial colonies grown (CFU), multiplied by the dilution factor and expressed as CFU mL^{-1} of the suspension under test. European Standards for chemical disinfectants and antiseptics (EN 14885) require the expression of the reduction in cell viability in the form of $R \log_{10}$. Thereby, results are expressed in CFU counts N_t at a contact time t (N_0 at $t = 0$), in percent reduction in cell viability $[(N_0 - N_t) \times 100]/N_0$ as well as in $R \log_{10}$ reduction ($R = \log_{10}(N_0/N_t)$). The experiments were repeated two times for each tested strain. For each contact time tested, control numerations of CFU mL^{-1} were also performed in sterile distilled water and without particles. The cell viability was preserved for both bacteria under these conditions with CFU counts N_t at $t = 15$, 30, 60 and 180 min remaining constant regarding the counts N_0 at $t = 0$ min.

2-5) EPR spin trapping experiments

The stock suspensions of $Cu(OH)_2$ and $Cu_{0.9}Mg_{0.1}(OH)_2$ nanoparticles (2 mg mL^{-1}) were prepared in deionised water. The spin trapping agent DMPO and hydrogen peroxide were dissolved in deionised water. The EPR spectra of nanoparticles in X-band (modulation frequency of 100 kHz) were measured by means of EMXplus spectrometer (Bruker) with a High Sensitivity Probe-head (Bruker) in the Wilmad® quartz (CFQ) EPR tubes (O.D. = 2 mm, L = 100 mm) at 20 °C (data not shown); the experiments with the aqueous suspensions were performed using a small quartz flat cell (WG 808-Q, Wilmad-LabGlass). The suspensions containing nanoparticles at concentration of 2 mg mL^{-1} were mixed with DMPO and H_2O_2 stock solutions 2 min before recording the first EPR spectrum at 20 °C. In that way, the final concentration in nanoparticles within the analyzed suspension is 1 mg mL^{-1} as used in the bactericidal tests. The EPR spectra of DMPO-adducts were recorded every 5 min to follow their evolution during the first 20 min (4 consecutive recordings). Each spectrum is obtained by the accumulation of 10 scans of 30 seconds each. The experiments were repeated at least in triplicate. The g-values of DMPO spin-adducts were determined with an uncertainty of ± 0.0001 using a nuclear magnetic resonance teslameter and integrated frequency counter. The concentration of DMPO spin-adducts was evaluated from the double-integrated EPR spectra based on the calibration curve obtained from the EPR spectra of TEMPOL solutions measured under strictly identical experimental conditions. The experimental EPR spectra were analyzed by WinEPR software (Bruker) and the simulated spectra were calculated using the EasySpin toolbox.[27] EPR spectrometer settings in the spin trapping experiments: microwave frequency, ~9.43 GHz; microwave power, 21.4 mW; center field, ~335.8 mT; sweep width, 8 mT; gain, 2.00×10^5; modulation amplitude, 0.05 mT or 0.1 mT; sweep time, 30 s; time constant, 5.12 ms; number of scans, 10.

3-Results and discussion

3-1) Synthesis and phase identification of nanoparticles

The synthesis of nanometer-sized $Cu(OH)_2$ particles is delicate because of its instability in hydroxide ion rich-medium conventionally used from the precipitation of hydroxide. Indeed, Cudennec *et al.*[28] observed that precipitation carried out at room temperature from a solution of copper salt with sodium hydroxide solution transiently gives rise to weakly crystallized particles of cupric hydroxide which quickly transform into CuO. For those authors, a progressive dissolution of $Cu(OH)_2$ particles occurs with time in hydroxide ion rich-medium, leading to the formation of the soluble square planar $[Cu(OH)_4]^{2-}$ complex. This anion is considered as the elementary building unit which enables the precipitation of cupric oxide by condensation/dehydration.[29] In addition, cupric hydroxide starts decomposing into CuO when heated above 145–160 °C.[30] Thereby, any hydrothermal treatment above 140 °C of a copper precursor in a protic solvent inevitably leads to cupric oxide particles.[31] This instability is directly related to singularities of the crystal structure of spertiniite $Cu(OH)_2$,[32] as evidenced by Cudennec *et al.*[33]

As detailed in the experimental section, nanometer-sized particles of $Cu(OH)_2$ were successfully prepared at room temperature by adding Na_2CO_3 to the precipitating sodium hydroxide. We observed that the addition of sodium carbonate delays the transformation of $Cu(OH)_2$ into CuO. Commercial copper nitrate has a degree of hydration that is not always constant. In order to control the concentration in cupric ions of the solution used for precipitation, copper nitrate was beforehand prepared from CuO by respecting some precautions explained hereafter. In a Teflon beaker, CuO (2.5 mmol) is first dissolved at room temperature in 20 mL of concentrated HNO_3. After homogenization for 30 min under stirring, the Teflon beaker is heated up to 140 °C in an oil bath to slowly evaporate the excess of nitric acid until a viscous blue liquid is obtained. By removing the beaker from the bath, a crystallization of a blue solid corresponding to $Cu(NO_3)_2{\cdot}xH_2O$ then occurs upon cooling. Prolonged heating of the blue viscous liquid to 140 °C causes decomposition of $Cu(NO_3)_2{\cdot}xH_2O$ into rouaite $Cu_2NO_3(OH)_3$.[34] This thermal decomposition must be avoided because the basic copper nitrate has a low solubility product constant in diluted nitrate medium ($K_{sp} = 1.92 \times 10^{-36}$ in 0.05 M KNO_3 solution[35]). All attempts to prepare nanometer-sized particles of magnesium-substituted $Cu(OH)_2$ (*i.e.* $Cu_{1-x}Mg_x(OH)_2$ with $0.05 \leq x \leq 0.2$) according to the above experimental protocol and by using $Mg(NO_3)_2{\cdot}6H_2O$ as magnesium source failed. Indeed, it was difficult to obtain a mixture of hydrated metal nitrates without decomposing $Cu(NO_3)_2{\cdot}xH_2O$ into rouaite $Cu_2NO_3(OH)_3$. To overcome this difficulty, magnesium and copper nitrates were replaced with the corresponding chlorides. Precipitation of $Cu(OH)_2$ nanoparticles can also be performed from a 0.5 M solution of $CuCl_2$ but the blue suspension tends to turn turquoise green color (or even darken further depending on the batch prepared, without any parameters of the synthesis being changed) during the ageing period. This darkening of the suspension is linked to the progressive conversion of $Cu(OH)_2$ into CuO, as evidenced by XRPD on the darkest powder. This method of preparing $Cu(OH)_2$ nanoparticles was discarded because the suspension is not stable from one synthesis to the next.

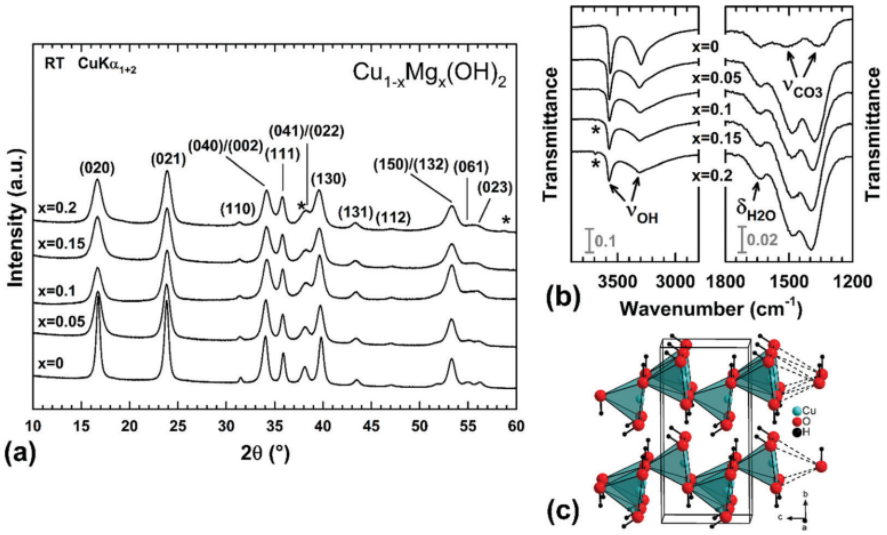

Fig. 1 Room-temperature (RT) XRPD patterns (a) IR transmission spectra (b) of $Cu_{1-x}Mg_x(OH)_2$ nanoparticles for different magnesium contents x. Very small peaks ascribed to the secondary $Mg(OH)_2$ phase are marked with an asterisk (*). (c) Perspective view of the crystal structure of $Cu(OH)_2$ with a description in terms of rectangular pyramidal coordination of cupric ions.

The phase purity of as-prepared powders was checked by recording XRPD patterns with the data collection conditions given in ESI† (Section S1.2). In Fig. 1a, the XRPD patterns of raw powders show single $Cu(OH)_2$-type phase (spertiniite) up to a magnesium content of $x = 0.15$. For $x = 0.2$, a small trace of $Mg(OH)_2$ is detected (a shoulder and one peak respectively at around 38° and 59° in 2θ marked with an asterisk in Fig. 1a), thus indicating that the limit of the solid solution $Cu_{1-x}Mg_x(OH)_2$ is exceeded.

Infrared spectra were collected at room temperature on those raw powders (data collection conditions given in Section S1.3 of ESI†). Fig. 1b shows the superimposition of the different spectra as a function of the magnesium content x. In each IR spectrum, two intense stretching vibration bands of hydroxyl groups[36] (ν_{OH} in Fig. 1b) are observed at around 3560 and 3300 cm^{-1}, respectively. In addition to these two bands, the IR spectrum of the $x = 0.2$ sample shows a third ν_{OH} band of very weak intensity at 3700 cm^{-1} (marked with an asterisk in Fig. 1b) which is ascribed to the presence of the secondary phase $Mg(OH)_2$.[37] In the crystal structure of $Cu(OH)_2$,[32] cupric ions are 5-fold coordinated to hydroxide ions, thus forming pyramids $[Cu(OH)_5]^{3-}$ (Fig. 1c). Within these pyramids, Cu^{2+} ions are displaced by 0.134 Å from the rectangular base (Cu–O equatorial bonds 2 × 1.948(3) Å and 2 × 1.972(3) Å). The pyramids are highly distorted since the Cu^{2+} ions are 2.356(5) Å away from the apical hydroxide ion. One hydroxide ion, located on the other side of the rectangular base of the $[Cu(OH)_5]^{3-}$ pyramid, is too far away from cupric ion (2.915(5) Å) to be part of a coordination octahedron (dashed lines in Fig. 1c). Pyramids share opposite edges of their rectangular bases to form infinite $[Cu(OH)_3]^-_\infty$ ribbons running along the crystallographic a direction. Each ribbon of pyramids are translated by the vector $1/2\vec{a} + 1/8\vec{b}$ in such a way that the apical hydroxide ions of one ribbon form the external HO–OH edges of the neighboring one. A staircase-shaped $[Cu(OH)_2]_\infty$ layer of pyramids is thus built up (Fig. 1c). The hydroxide ions point out of both sides of each $[Cu(OH)_2]_\infty$ layer towards oxygen atoms of the two adjacent layers. Hydrogen bonds thus formed ensure the periodic stacking of those staircase-shaped layers along the b direction which are thereby spaced by infinite bi-dimensional corrugated galleries parallel to the (a, c) plane.

In a single staircase-shaped $[Cu(OH)_2]_\infty$ layer (Fig. 1c), three of the five hydroxide ions defining the vertices of each $[Cu(OH)_5]^{3-}$ pyramid are shared with two other neighbouring coordination polyhedra (triple-shared or $[(OH)Cu_3]^{5+}$ environment), while the remaining two hydroxide ions are connected to one neighbouring coordination polyhedron only (double-shared or $[(OH)Cu_2]^{3+}$ environment). Two non-equivalent hydroxide ions then coexist in the crystal structure of $Cu(OH)_2$, thus explaining the presence of two distinct stretching vibration ν_{OH} bands in the IR spectrum. The frequency of ν_{OH} vibration decreases as the hydroxide ions multiply their connections to cupric ions. Thereby, the stretching vibration bands at frequencies of 3300 and 3560 cm^{-1} are ascribed to triple-shared and double-shared hydroxide ions, respectively. In Fig. 1b, three very weak vibration bands emerge at 1650, 1500 and 1400 cm^{-1} from the background of the IR spectrum of $Cu(OH)_2$ sample. The first band at around 1650 cm^{-1} corresponds to the bending vibration δ of water molecules[36] adsorbed in a very low amount at the surface of the $Cu(OH)_2$ nanoparticles (δ_{H_2O} in Fig. 1b). No vibration band for adsorbed CO_2 molecules is observed at 2350 cm^{-1} in the IR spectra

(not shown in Fig. 1b). Thereby, the two weak bands at 1500 and 1400 cm^{-1} are attributed to the asymmetric stretching vibrations ν of C–O bonds in carbonate groups CO_3^{2-} [36] (ν_{CO_3} in Fig. 1b) coordinated to terminal Cu^{2+} cations at the surface of $Cu(OH)_2$ nanoparticles. These adsorbed carbonate groups could come either from the reactive adsorption of CO_2 molecules from the ambient air or from the alkaline $NaOH/Na_2CO_3$ medium used to precipitate cupric hydroxide. In Fig. 1b, the intensity of these two ν_{CO_3} bands significantly increases with increasing the magnesium content x in the $Cu_{1-x}Mg_x(OH)_2$ samples. This is linked to the presence of basic Mg site at the surface of particles, whose amount increases with x. The asymmetric stretching vibration ν of C–O bonds in the free CO_3^{2-} ion (D_{3h} symmetry) gives rise to one active IR band at 1415 cm^{-1}.[38] These carbonate groups can be mono- or bi-coordinated to terminal divalent cations at the surface of nanoparticles, as observed for MgO or CaO.[38] Whatever the coordination of those adsorbed carbonate groups, their three C–O bonds are no more equivalent as in the free CO_3^{2-} ion. Thus, the IR band of the free CO_3^{2-} ion at 1415 cm^{-1} splits into two bands as we observed in Fig. 1b. The difference $\Delta\nu$ in position of these two bands can be as high as 100 cm^{-1} for a mono-coordination and around 300 cm^{-1} for a bi-coordination of CO_3^{2-} ions.[38] Because the difference $\Delta\nu$ does not exceed 100 cm^{-1} in Fig. 1b, one can conclude that the carbonate groups are mono-coordinated to terminal divalent cations (Mg and Cu) at the surface of nanoparticles. In Fig. 1a, no carbonate or hydroxide carbonate are detected as secondary phase by XRPD, even at trace level, under the data collection conditions used (Section S1.2 in ESI†). This is consistent with the very weak adsorption of carbonate groups onto the surface of nanoparticles evidenced by IR spectroscopy.

The thermal decomposition of each $Cu_{1-x}Mg_x(OH)_2$ sample has been monitored by ThermoGravimetric (TG)-Mass Spectrometric (MS) evolved gas analyses and temperature-controlled XRPD to provide information about the transformation process and the chemical composition (data collection conditions given in Sections S1.4 and S1.2 of ESI,† respectively). Thermograms, mass spectra and thermal evolutions of diffraction patterns for three selected samples x = 0, 0.1 and 0.2 are both displayed in Fig. 2. Thermograms and mass spectra recorded on the two remaining samples of the series (x = 0.05 and 0.15) are shown in ESI† (Fig. S2 in Section S2). The thermogram of the parent compound $Cu(OH)_2$ exhibits first a continuous weight loss up to ≈125 °C attaining ≈0.55% in magnitude (Fig. 2). Temperature-controlled diffraction reveals that cupric hydroxide is preserved below 125 °C (Fig. 2). Although that no distinct bump is observed in the m/z = 18 spectrum below 125 °C, this first weight loss is attributed to a progressive desorption of water molecules from the surface of $Cu(OH)_2$ nanoparticles whose presence was evidenced by IR spectroscopy at room temperature (a weak bending vibration band δ_{H_2O} of adsorbed water molecules in Fig. 1b). As the temperature increases, an abrupt and large weight loss suddenly occurs between 125–200 °C. A very intense narrow peak and a much weaker one are observed at around 155 °C in the m/z = 18 and m/z = 44 spectra, respectively (Fig. 2). This is in very good agreement with the value of the endothermic peak (peak max at 151 °C) determined by Tanaka *et al.*[39] from TG-DSC measurements performed on $Cu(OH)_2$ at the same heating rate as ours (*i.e.* 2 °C min^{-1}). This weight loss is therefore associated to the simultaneous releases of water and a few carbon dioxide molecules.

Above 200 °C, the sample mass still continues to weakly decrease up to 700 °C although that no bump is clearly detected on both mass spectra in this temperature range. The weight loss cumulatively reaches ≈18.75% between 125–700 °C. At 125 °C (the onset temperature of the decomposition determined by TG-MS analysis), a coexistence of $Cu(OH)_2$ and CuO phases is evidenced by temperature-controlled diffraction (pattern in pink color in Fig. 2). Only Bragg peaks of CuO are present in the diffraction patterns collected above this temperature. Thereby, the weight loss between 125–700 °C results from the thermal decomposition of cupric hydroxide into CuO. IR spectroscopy showed that a few carbonate groups are mono-coordinated to terminal Cu^{2+} cations at the surface of $Cu(OH)_2$ nanoparticles. Those carbonate groups decompose along with nanoparticles by releasing gaseous CO_2 molecules. Theoretically, a weight loss of 18.5% is expected for the decomposition reaction $Cu(OH)_2 \rightarrow CuO + H_2O$ which means that the extra loss of 0.25% (supplement to 18.75%) corresponds to the release of CO_2.

Cudennec *et al.*[33] demonstrated that the formation of CuO through the dehydroxylation of cupric hydroxide requires the displacements of staircase-shaped $[Cu(OH)_2]_\infty$ layers in the (a, c) plane with respect to each other in order to form new O–Cu–O bridges between the former layers along the b-axis (oxolation process) as the gaseous water molecules are released (see Fig. 1c for better understanding). During dehydroxylation, lattice strains naturally appear at the reaction interface between just oxolated and still hydroxylated layers due to the local reduction of the packing Cu–Cu distance along the initial b-axis of the crystal structure of $Cu(OH)_2$. Dehydroxylation starts at the edges of particle and progresses to the particle core. When it exceeds the tensile strength of particle, the accumulation of lattice strains causes nanoscale cracks which start propagating in the entire particle. After a short period of reaction, several nanodomains of CuO break away from the matrix. This behaviour is similar to that observed for the thermal decomposition of magnesium hydroxide into MgO.[40] It explains why a halving of the "particle size" ("coherently diffracting nanodomains" would be more accurate) was noted by Fukuda *et al.*[41] in the course of the decomposition of $Cu(OH)_2$ into CuO. Our TG analysis shows that this process is very rapid. This inevitably generates nanoscale voids between the different nanodomains into which a few gaseous water molecules (and even CO_2 molecules) may remain trapped. As the annealing temperature increases from 200 to 400 °C, the coherently diffracting nanodomains weld together and grow in size leading to the reduction in full-width at half maximum (FWHM) of the diffraction peaks of CuO as noted in Fig. 2. The long tail observed from 200 to 700 °C in the TGA thermogram (Fig. 2) indicates that the trapped H_2O/CO_2 molecules are

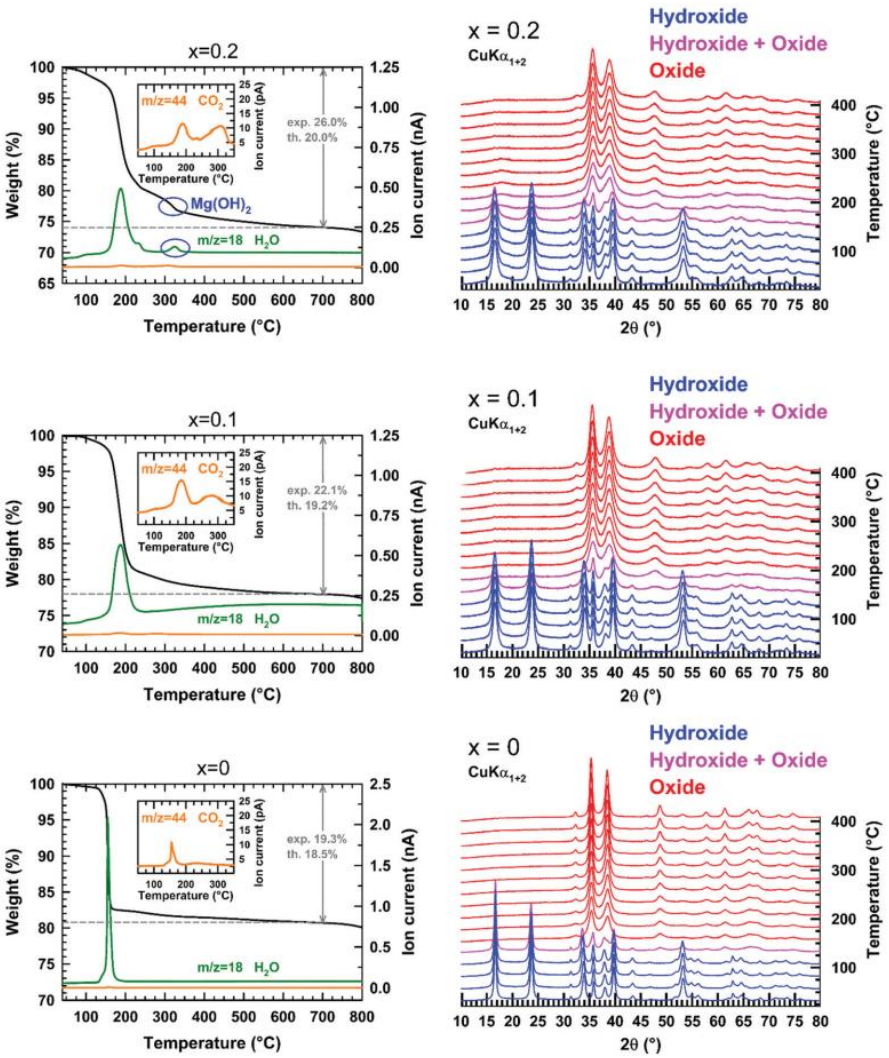

Fig. 2 (left) TGA thermograms and mass spectra of released water and carbon dioxide collected upon heating in argon on $Cu(OH)_2$ (x = 0), $Cu_{0.9}Mg_{0.1}(OH)_2$ (x = 0.1) and $Cu_{0.8}Mg_{0.2}(OH)_2$ (x = 0.2) raw powder samples. (right) Thermal evolution of the XRPD patterns of the same samples when annealed in air from RT to 400 °C.

progressively expelled from nanoscale voids when the nanodomains weld together. Fukuda *et al.*[41] came to the same interpretation of the tail in their TGA thermogram of $Cu(OH)_2$.

In Fig. 2 and Fig. S2 (ESI†), the $Cu_{0.95}Mg_{0.05}(OH)_2$ and $Cu_{0.9}Mg_{0.1}(OH)_2$ samples behave the same way as $Cu(OH)_2$ upon heating: a single step thermal decomposition into the corresponding mixed $Cu_{1-x}Mg_xO$ oxide is observed with a tail running up to 700 °C. A progressive broadening and decrease in intensity of the peak associated to the release of water molecules in the m/z = 18 spectra is however noted as the magnesium content x increases in the samples. This leads to the shift in position of the peak maximum towards higher temperatures (171 and 187 °C for x = 0.05 and 0.1, respectively). This time, the release of CO_2 molecules clearly occurs in two steps since two broad peaks are observed in the m/z = 44 spectra of both $Cu_{0.95}Mg_{0.05}(OH)_2$ and $Cu_{0.9}Mg_{0.1}(OH)_2$ samples (Fig. S2 in ESI† and Fig. 2). At the same time, the tail of the TG curves becomes more pronounced as the magnesium content x increases in the samples. This is especially the case in the temperature range 200–300 °C where the second peak appears in the m/z = 44 spectra. More CO_2 molecules seem to be trapped in nanoscale voids between nanodomains of $Cu_{1-x}Mg_xO$. This is probably related to the presence of basic Mg sites at the surface of nanodomains, whose amount increases with x. For the

$Cu_{0.8}Mg_{0.2}(OH)_2$ sample, the tail of the TG curve exhibits a step in the temperature range 300–350 °C and a peak simultaneously appears at 325 °C in the m/z = 18 spectrum (blue circles in Fig. 2). A secondary phase $Mg(OH)_2$ was detected by XRPD and IR spectroscopy in the raw $Cu_{0.8}Mg_{0.2}(OH)_2$ sample (Fig. 1). In our previous study,[37] TG-MS evolved gas analyses showed that nanoplatelets of $Mg(OH)_2$ starts decomposing above 300 °C by releasing water molecules (peak at 350 °C in the m/z = 18 spectrum). The step in the tail of the TG curve of the $Cu_{0.8}Mg_{0.2}(OH)_2$ sample is therefore ascribed to the thermal decomposition of this secondary phase $Mg(OH)_2$. A soft step in the TGA thermogram of the $Cu_{0.85}Mg_{0.15}(OH)_2$ sample with a low-intensity peak in the m/z = 18 spectrum is surprisingly observed in the temperature range 300–350 °C (Fig. S2, ESI†). This means that $Mg(OH)_2$ is also present in the x = 0.15 sample but in an amount too small to be detectable by XRPD (Fig. 1a), under the data collection conditions used (Section S1.2 in ESI†). Close examination of the IR spectrum of x = 0.15 sample reveals that the stretching ν_{OH} vibration at 3700 cm^{-1}, characteristic of $Mg(OH)_2$, emerges slightly from the baseline (marked with an asterisk in Fig. 1b). The limit of the solid solution $Cu_{1-x}Mg_x(OH)_2$ is therefore located between x = 0.1 and 0.15.

Refinements of the crystal structures of the different $Cu_{1-x}Mg_x(OH)_2$ hydroxides were attempted from those XRPD patterns by the Rietveld method[42] of the Fullprof program[43] using the orthorhombic crystal structure of spertiniite $Cu(OH)_2$, as a starting structural model.[32] The profile shape of all Bragg reflections located at scattering angles higher than 50° in 2θ remains unsatisfactorily modelled by least-squares fitting this structural model. This problem is due to the small size of the coherently diffracting domains within the $Cu_{1-x}Mg_x(OH)_2$ particles which considerably broadens all the Bragg peaks making them overlap and reducing their intensity. However, all the Bragg peaks have a symmetric Voigt-type profile which makes possible a microstructural analysis from XRPD data using the Integral Breadth method,[44–47] as described in details in Section S1.2 of ESI.† In the present analysis, the peak broadening is assumed to originate from both the nanometer size (the "size broadening" effect) and the lattice distortion ("microstrain broadening" effect) of coherently diffracting domains. For each $Cu_{1-x}Mg_x(OH)_2$ sample, the a, b and c parameters of the orthorhombic unit cell together with the apparent size S_β and the average lattice strain $\langle\varepsilon_\beta\rangle$ of those nanodomains were determined from the refinement of the XRPD patterns by the Le Bail method[48] of the Fullprof program.[43] Note that, the presence of $Mg(OH)_2$ as secondary phase was taken into account in the refinement of the XRPD patterns of the $Cu_{0.85}Mg_{0.15}(OH)_2$ and $Cu_{0.8}Mg_{0.2}(OH)_2$ samples. As shown in Fig. 3a for $Cu_{0.9}Mg_{0.1}(OH)_2$, the experimental diffraction

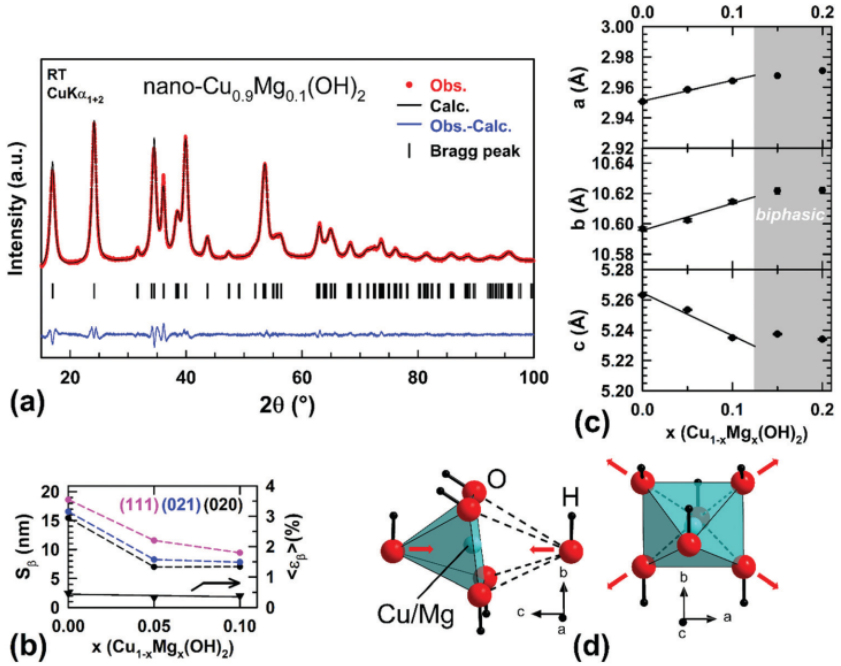

Fig. 3 (a) Comparison of the observed diffraction pattern of $Cu_{0.9}Mg_{0.1}(OH)_2$ (x = 0.1) nanoparticles (red dots) with the pattern calculated by the Integral Breadth method (black line). The blue curve corresponds to the difference between observed and calculated patterns. Vertical markers give Bragg peak positions of the orthorhombic space group $Cmc2_1$ (No. 36). (b) Variations of the average lattice strain $\langle\varepsilon_\beta\rangle$ and the apparent size S_β of the coherently diffracting domains along different crystallographic directions with the magnesium content x in $Cu_{1-x}Mg_x(OH)_2$ nanoparticles. (c) Orthorhombic cell parameters of the $Cu_{1-x}Mg_x(OH)_2$ compounds for each magnesium content x. (d) Effects of the Mg substitution on the length of (Cu,Mg)–OH bonds within $[(Cu,Mg)(OH)_5]^{3-}$ pyramids marked with red arrows.

pattern can be satisfactorily fitted by using the Integral Breadth method. The values of the *a*, *b* and *c* parameters of each $Cu_{1-x}Mg_x(OH)_2$ sample as well as the conventional reliability factors are reported in Table S1 (Section S3 in ESI†). The variations of S_β, $\langle\varepsilon_\beta\rangle$ and the *a*, *b* and *c* parameters are shown in Fig. 3b and c as a function of the magnesium content *x* in the $Cu_{1-x}Mg_x(OH)_2$ nanoparticles. In Fig. 3b, the apparent size S_β in all crystallographic directions dropped by half as soon as the sample contains 5 mol% of magnesium and does not evolve for higher content *x*. In contrast, microstrains are invariant to the magnesium content *x* of the $Cu_{1-x}Mg_x(OH)_2$ hydroxide with a lattice strain ε_β remaining around 0.4% in average (Fig. 3b).

In the crystal structure of $Cu(OH)_2$,[32] cupric ions are 5-fold coordinated to hydroxide ions (Fig. 1c). When five-fold coordinated to hydroxide ions, Mg^{2+} ion (ionic radius = 0.66 Å (CN = 5)[49]) is slightly larger in size than the cupric cation (ionic radius = 0.65 Å (CN = 5)[49]). Within the compositional range $0 \leq x \leq 0.1$, a progressive increase of the cation–OH bond lengths with *x* is therefore expected in average which should in turn expand the unit cell along the three crystallographic directions. While the unit cell linearly expands in the basal (*a*, *b*) plane, a regular contraction surprisingly occurs along the *c*-axis in the range $0 \leq x \leq 0.1$ (Fig. 3c). These evolutions of the three cell parameters therefore follow usual Vegard's laws[50] in the range $0 \leq x \leq 0.1$. For each cell parameter, a departure from linearity with a kind of levelling off is observed above $x = 0.1$. This shows that the limit of the solid solution $Cu_{1-x}Mg_x(OH)_2$ is between $x = 0.1$ and 0.15, as earlier suggested by the TG-MS analyses of the $x = 0.15$ and 0.2 samples.

Although no satisfactory Rietveld refinement of the crystal structure could be carried out for the different $Cu_{1-x}Mg_x(OH)_2$ hydroxides, an explanation for the evolutions of cell parameters previously observed can nevertheless be proposed. In the structure of $Cu(OH)_2$,[32] the coordination $[Cu(OH)_5]^{3-}$ pyramids are highly distorted (Fig. 1c) with one long apical Cu–OH distance (2.356(5) Å) and four short equatorial Cu–OH distances (2 × 1.948(3) Å and 2 × 1.972(3) Å). A sixth hydroxide ion, located on the other side of the rectangular base of the $[Cu(OH)_5]^{3-}$ pyramid, is too far away from cupric ion (2.915(5) Å) to be part of a coordination octahedron (dashed lines in Fig. 1c and 3d). Note that, these Cu–OH bond lengths are much longer or slightly shorter than the sum of ionic radii $r_{Cu} + r_{OH}$ ($\approx$1.98 Å for $[Cu(OH)_5]^{3-}$ to 2.07 Å for $[Cu(OH)_6]^{4-}$ by taking into account the cationic environments of the different OH ligands[49]). This distortion of the [4+1] or [4+2] coordination polyhedra is characteristic of a Jahn–Teller effect of Cu^{2+} ion ($3d^9$). At reverse, Mg^{2+} ion cannot generate such distortion because of its electronic configuration. When incorporated in the cationic sub-lattice of $Cu(OH)_2$, Mg^{2+} ions will tend to be six-fold coordinated to hydroxide ions rather than five-fold. As in $Mg(OH)_2$, the $[Mg(OH)_6]^{4-}$ octahedron should be quite regular with Mg–OH bond lengths corresponding roughly to the sum of ionic radii $r_{Mg} + r_O = 2.06$ Å (with hydroxide ions in $[(OH)Mg_3]^{5+}$ environment[49]). Consequently, the replacement of a few elongated $[Cu(OH)_6]^{4-}$ octahedra by more regular $[Mg(OH)_6]^{4-}$ ones necessarily shortens on average the two apical (Mg,Cu)–OH bond lengths, as shown by the red arrows in Fig. 3d. The contraction of the unit cell parameter *c* upon substitution (Fig. 3c) reflects this shortening because the apical (Mg,Cu)–OH bonds are all oriented along the *c*-axis in the $[(Cu/Mg)(OH)_2]_\infty$ layers of octahedra (Fig. 1c and 3d). The equatorial rectangles of octahedra are all parallel to the basal (*a*, *b*) plane. The increase of both unit cell parameters *a* and *b* upon substitution means that the four mean equatorial (Cu,Mg)–OH distances within octahedra increase (red arrows in Fig. 3d). Note that, the two apical OH groups of each $[Cu(OH)_6]^{4-}$ octahedron form the equatorial rectangles of the next neighboring polyhedra in the crystal structure of $Cu(OH)_2$ (Fig. 1c). Thus, the magnesium substitution causes the displacement of half of the hydroxide ions along the [111] direction while the other half moves in the opposite direction (*i.e.* [11–1] direction), as depicted in Fig. 3d. Any shortening of the two apical (Mg,Cu)–OH bonds necessarily leads to a lengthening of the four equatorial (Mg,Cu)–OH bonds. This univocally explains why the unit cell parameter *c* has an opposite evolution with *x* to those of the parameters *a* and *b*.

Since the limit of the solid solution $Cu_{1-x}Mg_x(OH)_2$ is between $x = 0.1$ and 0.15, the next sections mainly focus on the three single-phase samples $Cu(OH)_2$, $Cu_{0.95}Mg_{0.05}(OH)_2$ and $Cu_{0.9}Mg_{0.1}(OH)_2$ only. Before evaluating the bactericidal activity of these three compositions, the morphology and the size of their nanoparticles were determined by transmission electron microscopy (TEM). The following section is devoted to this investigation.

3-2) Morphology and size of nanoparticles

The TEM images of the nanometer-sized particles of $Cu(OH)_2$, $Cu_{0.95}Mg_{0.05}(OH)_2$ and $Cu_{0.9}Mg_{0.1}(OH)_2$ are shown in Fig. 4. All nanoparticles have a rod-like shape with a diameter of about 15 nm whether they contain (Fig. 4b–d) or not (Fig. 4a) magnesium ions. However, the length of these rods is approximately 100–200 nm for both magnesium-containing hydroxides $x = 0.05$ and $x = 0.1$ while it reaches several hundred nanometers for the parent compound $x = 0$. Note that, a huge difference exists between the size of $Cu_{1-x}Mg_x(OH)_2$ nanorods measured from TEM micrographs and the apparent size S_β of the coherently diffracting domains calculated along different crystallographic directions from XRPD patterns (Fig. 3b). In Fig. 4c, a single nanorod, representative of the $x = 0.05$ powder, was observed at higher magnification by TEM. The grainy appearance together with the irregular contrast changes at the edge demonstrate that each nanorod appearing on TEM images is made up of an assembly of several coherently diffracting domains with different orientations.

Nitrogen sorption measurements were also carried out to determine the specific surface areas (SSA) of those powders (data collection conditions given in Section S1.6 of ESI†). Powders of magnesium-containing hydroxides both have a SSA of $\approx$80 $m^2\ g^{-1}$ (Fig. 4b and d) due to a similar disordered aggregation of nanorods. Curiously, the long nanorods within the powder of $Cu(OH)_2$ are strongly agglomerated into bundles,

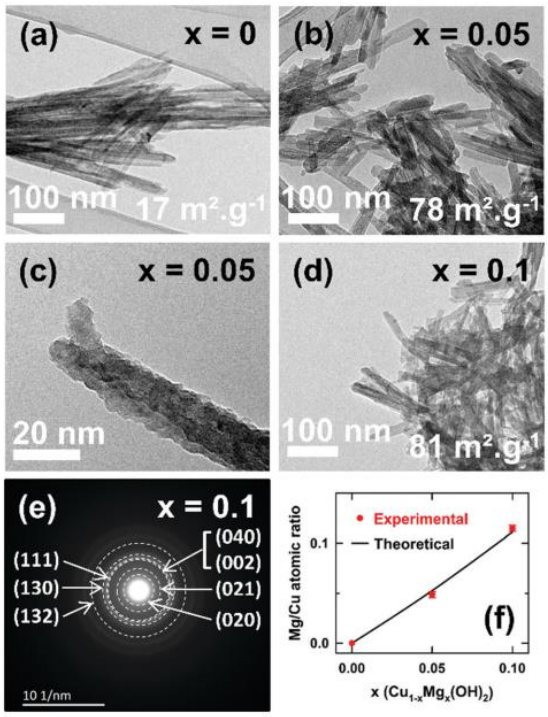

Fig. 4 (a–d) TEM micrographs of $Cu_{1-x}Mg_x(OH)_2$ nanorods for different magnesium contents x. Specific surface area determined from N_2 adsorption measurements are given. (e) SAED pattern of several $Cu_{0.9}Mg_{0.1}(OH)_2$ nanorods (x = 0.1). (f) Evolution of the Mg/Cu atomic ratio determined by EDX analysis as a function of the nominal magnesium content x in $Cu_{1-x}Mg_x(OH)_2$ nanorods.

thus leading to a low SSA of $\approx$17 m^2 g^{-1} (Fig. 4a). Note that, $Cu(OH)_2$ nanorods prepared from $Cu(NO_3)_2{\cdot}xH_2O$ and $CuCl_2$ have the same degree of agglomeration on TEM images (not shown). Therefore, SSA values and TEM images suggest that magnesium substitution tends to reduce both agglomeration and length of nanorods. For each hydroxide, the selected area electron diffraction (SAED) pattern collected on several nanorods show six distinct rings, as shown in Fig. 4e for the x = 0.1 sample. The presence of rings rather than individual diffraction spots results from the superimposition of the SAED patterns of the numerous nanorods analyzed at the same time. These six rings are indexed to the crystal planes (020), (021), (040)/(002), (111), (130) and (132) of a $Cu(OH)_2$-type structure with interreticular d_{hkl} distances in very good agreement with those of the six most intense Bragg diffraction peaks in the XRPD patterns displayed in Fig. 1a. It thus confirms the high crystallinity of the nanorods of $Cu_{1-x}Mg_x(OH)_2$ we synthesized. For each nano-$Cu_{1-x}Mg_x(OH)_2$ hydroxides, the magnesium to copper atomic ratio, determined by EDX analysis carried out on several single nanorods, is in very good agreement with the nominal ratio (Fig. 4f).

3-3) Bactericidal activity

The bactericidal activity of $Cu_{1-x}Mg_x(OH)_2$ nanorods against *E. coli* and *S. aureus* was evaluated at 20 °C in sterile distilled water with a concentration in particles of 1 mg mL^{-1}. For each $Cu_{1-x}Mg_x(OH)_2$ hydroxide tested, the sterile water suspension of particles in contact with a bacterial strain (final concentration at $\approx 10^6$ CFU mL^{-1}) was maintained at 20 °C for 15, 30, 60 and 180 min under controlled shaking speed. After each contact time t, a counting of the number N_t of CFU was performed to estimate the reduction in cell viability in comparison to N_0. For both *E. coli* and *S. aureus*, the $R\log_{10}$ and the percent reductions in cell viability at the different time in contact with $Cu_{1-x}Mg_x(OH)_2$ nanorods are displayed as a function of the magnesium content x in Table 1.

The results, presented in Table 1, show that 100% reductions in viability of *E. coli* ($>6\log_{10}$) are achieved after 180 min on contact with nanorods of $Cu(OH)_2$, $Cu_{0.95}Mg_{0.05}(OH)_2$ and $Cu_{0.9}Mg_{0.1}(OH)_2$. Although the reductions in viability of *S. aureus* reach 99.3 and 99.98% ($\approx$3 and 4 $\log_{10}$) after 180 min on contact with $Cu_{0.95}Mg_{0.05}(OH)_2$ and $Cu_{0.9}Mg_{0.1}(OH)_2$ nanorods respectively, they remain below those reported for *E. coli* at the same specified contact time. Only $Cu(OH)_2$ exhibits comparable bactericidal activities against both *E. coli* and *S. aureus* after 180 min, since the nanorods kill the entire initial inocula (100% reductions). For contact times of less

Table 1 Bactericidal activity of $Cu_{1-x}Mg_x(OH)_2$ nanorods (1 mg mL^{-1}) against *E. coli* CIP 53126 and *S. aureus* CIP 4.83 as a function of the magnesium content x (average value ± standard deviation over 2 assays)

		E. coli			*S. aureus*		
Magnesium content x	Contact time (min)	$\log_{10} N_0$	$\log_{10}(N_0/N_t)$	Reduction (%)	$\log_{10} N_0$	$\log_{10}(N_0/N_t)$	Reduction (%)
0	15	6.31 ± 0.02	1.36 ± 0.12	95.5 ± 1.2	6.20 ± 0.02	0.37 ± 0.05	57.5 ± 4.4
	30		2.00 ± 0.03	99.0 ± 0.1		0.52 ± 0.02	70.1 ± 1.3
	60		3.46 ± 0.17	99.96 ± 0.02		2.07 ± 0.02	99.2 ± 0.1
	180		6.31 ± 0.02	100		6.26 ± 0.01	100
0.05	15	6.72 ± 0.02	1.01 ± 0.28	88.1 ± 6.7	6.30 ± 0.05	0.33 ± 0.08	52.9 ± 8.3
	30		1.72 ± 0.48	96.8 ± 2.6		0.41 ± 0.06	61.1 ± 5.6
	60		3.22 ± 1.08	99.6 ± 0.4		1.07 ± 0.37	88.2 ± 8.2
	180		6.72 ± 0.02	100		2.88 ± 1.04	99.3 ± 0.7
0.10	15	6.72 ± 0.02	0.95 ± 0.33	85.4 ± 9.4	6.63 ± 0.11	0.97 ± 0.06	89.2 ± 1.4
	30		1.55 ± 0.66	93.2 ± 6.2		1.27 ± 0.17	94.2 ± 2.2
	60		2.88 ± 1.42	98.2 ± 1.8		1.94 ± 0.28	98.6 ± 0.8
	180		6.72 ± 0.02	100		3.95 ± 0.45	99.98 ± 0.01

than 180 min, the bactericidal activities of the x = 0.05 and x = 0.10 samples against *E. coli* are lower than those of the parent compound (x = 0), with a tendency to slightly decrease as the magnesium content x increases. A positive effect of magnesium substitution on the bactericidal activities of $Cu(OH)_2$ towards *S. aureus* is nevertheless noted for contact times of less than 60 min. But $Cu(OH)_2$ shows an increase in $\log_{10}$ reduction of more than 4 orders of magnitude over the next 120 min allowing it to far exceed the performance of $Cu_{0.9}Mg_{0.1}(OH)_2$. Akhavan *et al.*[51] evaluated the bactericidal activity of nano-structured CuO layers grown on the surface of copper foil by immersion in a diluted sodium hydroxide solution (0 to 3×10^{-2} mol L^{-1}) maintained at 60 °C for 20 h. High antibacterial activity against *E. coli* (with a reduction in viability around $5\log_{10}$ or 99.999% after 90 min) was observed when a NaOH concentration of 3×10^{-2} mol L^{-1} was used. The presence of $Cu(OH)_2$ was detected by XRD in this very active CuO layer thus grown. Our study demonstrates that cupric hydroxide could have a significant contribution to the antibacterial activity of this heterogeneous $CuO/Cu(OH)_2$ layer.

The bactericidal activity of bi-phasic $Cu_{0.85}Mg_{0.15}(OH)_2$ and $Cu_{0.80}Mg_{0.20}(OH)_2$ samples was also evaluated towards *E. coli* and *S. aureus*. Table S2 in ESI† displays the results. As we previously showed,[37] $Mg(OH)_2$ nanoparticles have poorly bactericidal performances in the evaluation conditions we used. Its presence as secondary phase in the $Cu_{0.85}Mg_{0.15}(OH)_2$ and $Cu_{0.80}Mg_{0.20}(OH)_2$ samples only further increases the slowing down of the bactericidal kinetics of the mixed hydroxides. The reductions in viability of both *E. coli* and *S. aureus* after 180 min in contact with these nanoparticles are very similar with those of the end-composition x = 0.1 of the solid solution $Cu_{1-x}Mg_x(OH)_2$. Our study demonstrates that the decrease in the size of $Cu(OH)_2$ particles to about a hundred nanometers allows to meet the U.S. Food and Drug Administration standards for water disinfection[5] ($5\log_{10}$ or 99.999% removal value) in a processing time as short as 180 min.

3-4) Bactericidal mechanism

As mentioned in the introduction, it was expected that the bactericidal activity of $Cu(OH)_2$ nanoparticles in water should be very low or insignificant due to its insolubility. However, $Cu(OH)_2$ is as active against *E. coli* as or even more active against *S. aureus* than $Cu_{0.9}Mg_{0.1}(OH)_2$ after 180 min, although the latter should release more cupric ions into the water than the former. This result incited us to verify the concentration of the cupric ions released from both $Cu(OH)_2$ and $Cu_{0.9}Mg_{0.1}(OH)_2$ nanorods after their immersion in water for 180 min and for a much longer period of 1440 min. The concentrations of the supernatant in divalent cations (Mg^{2+} and Cu^{2+}) were quantified by atomic emission spectroscopy (AES) analyses. In parallel, the pH of the supernatant was measured at the same specified time used for evaluating bactericidal performances. The concentrations in cations and the pH values at the different immersion times are gathered together in Table 2.

Table 2 Time dependence evolutions of the pH and of the concentrations in magnesium and copper ions released by $Cu(OH)_2$ and $Cu_{0.9}Mg_{0.1}(OH)_2$ nanorods in water (1 mg mL^{-1})

	$Cu(OH)_2$		$Cu_{0.9}Mg_{0.1}(OH)_2$		
Immersion time (min)	pH	Cu^{2+} (mg L^{-1})	pH	Mg^{2+} (mg L^{-1})	Cu^{2+} (mg L^{-1})
0	5.7		6.2		
15	6.1		9.4		
30	6.7		9.43		
60	6.7		9.52		
180	6.86	0.36	10.01	2.46	1.99
480	6.2		9.51		
1440	6.16	2.57	9.52	3.09	0.38

A sudden increase of three pH units takes place in the first 15 minutes after the $Cu_{0.9}Mg_{0.1}(OH)_2$ nanorods are immersed in water. After 60 min of immersion, the pH of the supernatant stabilises between 9.5 and 10. In the same conditions, the pH for the water suspension of $Cu(OH)_2$ nanorods increases by only one unit, thus being close to neutrality after 180 min. The $Cu(OH)_2$ and $Cu_{0.9}Mg_{0.1}(OH)_2$ nanorods both exhibit 100% reductions in viability of *E. coli* after 180 min despite the difference of two pH units between their water suspensions. The pH of the supernatant is therefore not responsible for the high bactericidal of activity of the $Cu_{1-x}Mg_x(OH)_2$ hydroxides towards *E. coli*. The initial inoculum of *S. aureus* is fully eradicated after 180 min in contact with the $Cu(OH)_2$ nanorods at a neutral pH (100% or $>6\log_{10}$ reduction) whereas it is not the case with $Cu_{0.9}Mg_{0.1}(OH)_2$ nanorods at a basic pH (99.98% or $\approx 4\log_{10}$ reduction). This suggests that *S. aureus* may have some resistance to bactericidal agent in basic medium that *E. coli* does not. This assumption is consistent with the difference between the reductions in viability of *E. coli* (100% or $>6\log_{10}$ reduction) and *S. aureus* (99% or $2\log_{10}$ reduction) we observed after 180 min in contact with the platelet-like "$Mg_{0.85}Cu_{0.15}(OH)_2$" nanoparticles at pH $\approx$ 10.4.[37]

Only $\approx$0.06 and $\approx$0.4 wt% of the $Cu(OH)_2$ nanorods dissolve in water after 180 min and 1440 min, respectively (Table 2). As we expected, the incorporation of 10 mol% Mg^{2+} in the cationic sub-lattice of $Cu(OH)_2$ enhances the dissolution of nanorods in water by 5.5-fold increase the concentration in cupric ions released after 180 min. When the $Cu_{0.9}Mg_{0.1}(OH)_2$ nanorods start dissolving in water, the amount of released cupric ions should be proportional to that of released magnesium ions in compliance with the Mg/Cu ratio of 1/9 fixed by the composition. If it is respected, the copper concentration in the supernatant calculated from the magnesium concentration in Table 2 should be equal to $\approx$57.88 mg L^{-1} after 180 min of immersion. However, the concentration in Cu^{2+} ions measured by MP-AES in the supernatant is 29 fold lower than it should be. This would mean that a partial precipitation of $Cu(OH)_2$ from the released cupric ions occurs with the immersion time. Note that the solubility product constant of $Cu(OH)_2$ in pure water[23] is $K_{sp} = 2.2 \times 10^{-20}$. In Table 2, the pH of the supernatant is much higher than 5.7, the value above which cupric hydroxide starts precipitating for a concentration in solvated cupric ions

of 57.88 mg L^{-1}. Considering that ≈57.88 mg L^{-1} of cupric ions must have been released by the dissolution of $Cu_{0.9}Mg_{0.1}(OH)_2$ nanorods after 180 min and that only 1.99 mg L^{-1} remain in the supernatant, we conclude that 96.6 wt% of the cupric ions released in water would have precipitated into $Cu(OH)_2$. The immersion in water of $Cu_{0.9}Mg_{0.1}(OH)_2$ would lead *in fine* to the formation of $Cu(OH)_2$ as a single phase after a long enough time. However, this complete conversion has not been achieved after 180 min since 90 wt% of the $Cu_{0.9}Mg_{0.1}(OH)_2$ nanorods still remain in the water suspension (initially at a concentration of 1 mg mL^{-1} in particles). In addition, Table 2 shows that the $Cu_{0.9}Mg_{0.1}(OH)_2$ nanorods continue to slowly dissolve after 1440 min. The co-presence of $Cu(OH)_2$ nanoparticles could therefore have a contribution to the bactericidal activity of the $Cu_{0.9}Mg_{0.1}(OH)_2$ nanorods against both bacteria. This contribution cannot be predominant in the first 180 min of contact because the amount of $Cu(OH)_2$ nanoparticles precipitated is small, however.

The minimal inhibitory concentrations (MIC) of soluble cupric ions for *E. coli* and *S. aureus* are 25 mg L^{-1} and 12.5 mg L^{-1}, respectively.[20] It is well known that solvated cupric ions can catalyse the generation of ROS from aqueous H_2O_2 through a Fenton-like redox cycling between Cu^{2+} and Cu^+/Cu^{3+} ions[21,22] (eqn (1)–(5)).

$$Cu^{2+} + H_2O_2 \rightarrow Cu^+ + O_2^{\bullet-} + 2H^+ \quad (1)$$

$$Cu^+ + H_2O_2 \rightarrow Cu^{2+} + OH^- + HO^\bullet \quad (2)$$

$$Cu^+ + H_2O_2 \rightarrow Cu^{3+} + 2OH^- \quad (3)$$

$$Cu^{3+} + H_2O_2 \rightarrow Cu^{2+} + O_2^{\bullet-} + 2H^+ \quad (4)$$

$$Cu^{2+} + O_2^{\bullet-} \rightarrow Cu^+ + O_2 \quad (5)$$

To have a bactericidal effect through the ROS they produce, the concentration of soluble cupric ions must be equal to or greater than the MIC (minimal bactericidal concentration MBC ≥ MIC). The concentrations in Cu^{2+} released in water by the dissolution of the $Cu(OH)_2$ and $Cu_{0.9}Mg_{0.1}(OH)_2$ nanorods (Table 2) are much lower than the MIC (or MBC) for *E. coli* and *S. aureus*. The released cupric ions have therefore no bactericidal effect on *E. coli* and *S. aureus* in our investigation.

At this stage, neither the small increase in the pH of the supernatant nor the cupric and magnesium ions it contains can explain how bacteria are killed by these $Cu_{1-x}Mg_x(OH)_2$ nanorods. Cupric ions on the surface of nanorods could also catalyse the generation of free $O_2^{\bullet-}/HO_2^\bullet$ and $HO^\bullet$ radicals through a Fenton-like redox cycle (heterogeneous catalysis) as solvated Cu^{2+} ions do in solution (homogeneous catalysis[21,22]). Spin trapping technique provides the possibility to monitor and identify these reactive radical intermediates by their addition to a diamagnetic spin trap molecule (*i.e.* 5,5-dimethyl-1-pyrroline *N*-oxide, DMPO) to form a more stable radical-adduct detectable by EPR. In a previous study,[52] we showed that MgO and $Mg_{0.9}Cu_{0.1}O$ nanoparticles immersed in water can generate free $HO^\bullet$ and $O_2^{\bullet-}$ radicals by detecting the corresponding DMPO-adducts by EPR. Hydroxyl radical $HO^\bullet$ is the most active among all ROS because it can initiate a free radical chain reaction leading to extensive lipid and organic peroxide formation in aerobically living organisms (oxidative stress).[53] These toxic $HO^\bullet$ radicals produced by MgO and $Mg_{0.9}Cu_{0.1}O$ nanoparticles damage the cell membrane and cause its lysis. Suspecting a similar bactericidal mechanism for $Cu_{1-x}Mg_x(OH)_2$ nanorods, this technique was therefore used to show whether they actually produce such free radicals. The EPR spin trapping experiments were carried out with water suspensions of $Cu(OH)_2$ and $Cu_{0.9}Mg_{0.1}(OH)_2$ nanorods at the same concentration (1 mg mL^{-1}) as used in the bactericidal tests.

Low-intensity EPR signals were measured for both aerated water suspensions of $Cu(OH)_2$ and $Cu_{0.9}Mg_{0.1}(OH)_2$ nanorods containing DMPO spin trapping agent (Fig. S3 in Section S5, ESI†). Each experimental EPR spectrum can be satisfactorily fitted with three superimposed signals: (i) four-line signal of $^\bullet$DMPO–OH spin adduct (a_N = 1.507 ± 0.004 mT, a_H^β = 1.477 ± 0.007 mT, g = 2.0057),[54,55] (ii) six-line signal with parameters typical for DMPO-adduct with carbon-centered radical (a_N = 1.602 ± 0.005 mT, a_H^β = 2.331 ± 0.008 mT, g = 2.0055) and (iii) six-line signal compatible with $^\bullet$DMPO–C(O)R spin adduct (a_N = 1.493 ± 0.004 mT, a_H^β = 1.843 ± 0.004 mT, g = 2.0059).[56] As shown in Fig. 1b, few carbonate groups are mono-coordinated to terminal divalent cations (Mg and Cu) at the surface of nanorods. Carbonate $CO_3^{\bullet-}$ radicals (oxygen-centered radical anions) could be produced from the reaction of HCO_3^- anions with hydroxyl radicals $HO^\bullet$.[57] However, the rate constant for reaction of $HO^\bullet$ with bicarbonate ions (8.5×10^6 M^{-1} s^{-1} [58]) is lower than the rate constant for the trapping of $HO^\bullet$ by DMPO (3.4×10^9 M^{-1} s^{-1} [59]). Most hydroxyl radicals are thus rapidly trapped by DMPO. For $CO_3^{\bullet-}$ radicals that could still be produced, their detection in our experimental conditions is unlikely. Indeed, Zhang *et al.*[60] showed that $CO_3^{\bullet-}$ radicals promote the oxidation of the spin trap DMPO to $DMPO^{\bullet+}$ cation radicals which in turn easily reacts with water molecules to form the $^\bullet$DMPO–OH spin adduct. Thereby, the production of low concentration of carbon-centered radicals (and its corresponding DMPO-adducts) may reflect a partial decomposition of DMPO in contact with Cu^{2+} ions. As shown in Fig. 5b, the total concentration of DMPO-adducts monitored in both aerated water suspensions of $Cu(OH)_2$ and $Cu_{0.9}Mg_{0.1}(OH)_2$ nanorods is less than 1 μmol L^{-1} within the first 22 minutes after adding DMPO. The quantity of hydroxyl radicals produced in this way remains too small to be the cause of the very high reduction in cell viability we observed (Table 1).

Hydrogen peroxide is a by-product of the normal metabolism of oxygen in aerobically living organisms[61] and is present at millimolar concentration in the culture supernatant of *E. coli* and *S. aureus*[62] despite their catalase activity. Thus, the presence of hydrogen peroxide in the medium could play a crucial role in the bactericidal mechanism of the nanorods studied. Consequently, H_2O_2 was added to all aerated water suspensions of nanoparticles containing DMPO and the EPR spectra were recorded under the same conditions as above. Aqueous suspensions of $Cu(OH)_2$ and $Cu_{0.9}Mg_{0.1}(OH)_2$

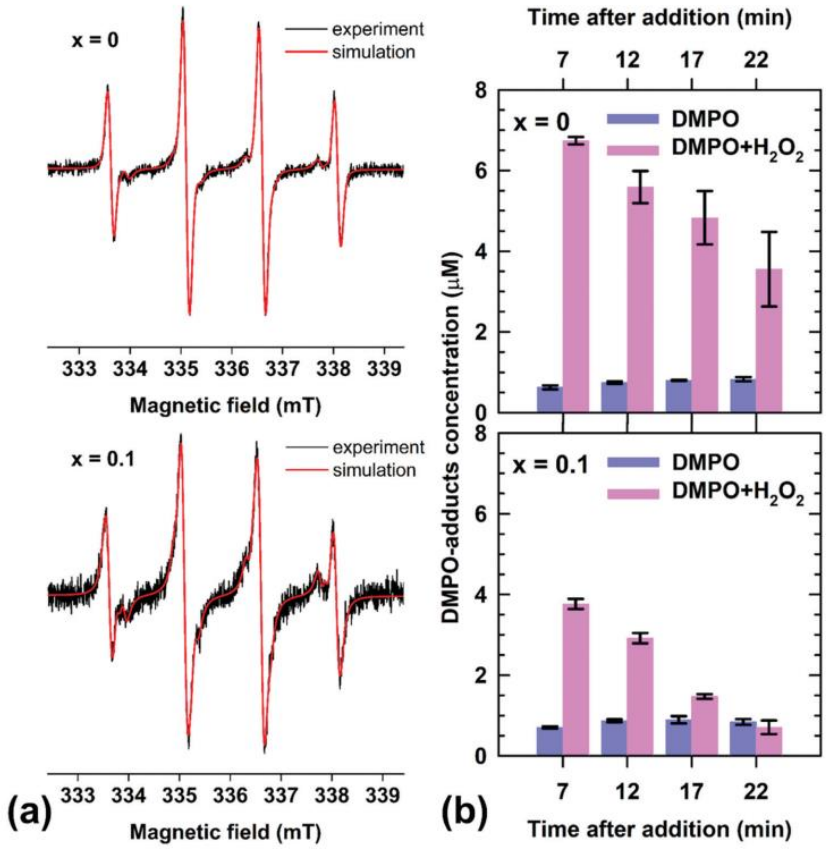

Fig. 5 (a) Normalized experimental (black line) and simulated (red line) EPR spectra measured 7 min after the addition of hydrogen peroxide ($c_0(H_2O_2)$ = 0.03 M) to the aerated water suspensions of $Cu(OH)_2$ (x = 0) and $Cu_{0.9}Mg_{0.1}(OH)_2$ (x = 0.1) nanorods (loading 1 mg mL^{-1}) in the presence of DMPO spin trapping agent (c_0(DMPO) = 0.04 M). The relative concentration of •DMPO-OH and •DMPO-O_2^-/O_2H spin adducts evaluated from the simulated spectra are as follows: $Cu(OH)_2$ (69.8% and 30.2%) and $Cu_{0.9}Mg_{0.1}(OH)_2$ (71.0% and 29.0%). (b) Time dependence of the total concentration of DMPO-adducts monitored at 20 °C with or without addition of H_2O_2 to the aerated water suspensions of the studied nanorods in the presence of DMPO.

nanorods containing H_2O_2 and DMPO exhibit very similar EPR spectra (Fig. 5a). Each experimental EPR spectrum can be satisfactorily fitted with two superimposed signals characterized by the spin-Hamiltonian parameters typical for two DMPO-adducts of oxygen-centered radicals, namely •DMPO-O_2^-/O_2H (12-line signal; a_N = 1.427 ± 0.017 mT, a_H^β = 1.141 ± 0.011 mT, a_H^γ = 0.140 ± 0.010 mT, g = 2.0058) and •DMPO-OH (4-line signal; a_N = 1.507 ± 0.004 mT, a_H^β = 1.477 ± 0.007 mT, g = 2.0057)[54,55] (Fig. 5a). Whether the water suspension of $Cu(OH)_2$ or $Cu_{0.9}Mg_{0.1}(OH)_2$ nanorods, the relative concentrations of •DMPO-OH and •DMPO-O_2^-/O_2H spin adducts are ≈70% and ≈30%, respectively (Fig. 5a). The magnesium substitution has therefore no effect on this ratio (at least up to a substitution rate of 10 mol%). In Fig. 5b, the addition of H_2O_2 to the water suspensions of $Cu(OH)_2$ and $Cu_{0.9}Mg_{0.1}(OH)_2$ nanorods induces a 10- or 5-fold increase in the total concentration of DMPO-adducts formed within the first 7 min, respectively. This figure also shows that, the total concentration of DMPO-adducts decreases with time in the absence of a new addition of H_2O_2 to suspensions: the decay being much faster for $Cu_{0.9}Mg_{0.1}(OH)_2$ nanorods than for $Cu(OH)_2$ ones. Thus, 22 min after H_2O_2 addition, the DMPO-adducts formed in contact with $Cu(OH)_2$ are 5 times higher in concentration than formed with $Cu_{0.9}Mg_{0.1}(OH)_2$, whereas this ratio was only 1.8 after 7 min. According to eqn (5), cupric ions are capable of converting superoxide $O_2^{\bullet-}$ radicals produced by Fenton-type reaction (eqn (1)) into molecular oxygen; this is consistent with the release of gas bubbles in the quartz flat cell containing nanorods during EPR measurements. The spin–spin interactions between DMPO-adducts and paramagnetic O_2 molecules is reflected in the EPR line broadening. Note that, the lines of the EPR signal are broader for $Cu_{0.9}Mg_{0.1}(OH)_2$ nanorods than those for $Cu(OH)_2$ ones (Fig. 5a). In Table 2, the concentration of cupric ions released by $Cu_{0.9}Mg_{0.1}(OH)_2$ nanorods is 5.5 times higher than by $Cu(OH)_2$ ones after 180 min. From the above observation, it appears that the more cupric ions are

released into the medium, the greater the conversion of superoxide $O_2^{\bullet-}$ radicals into O_2 molecules. Even if the relative concentration of $^{\bullet}$DMPO-O_2^{-}/O_2H spin-adduct measured after 7 min for suspensions of $Cu_{0.9}Mg_{0.1}(OH)_2$ nanorods (29%, Fig. 5a) is slightly smaller than that of $Cu(OH)_2$ ones (30.2%, Fig. 5a), the conversion rate of superoxide $O_2^{\bullet-}$ radicals is too limited to first drop by half the total concentration in DMPO-adducts after 7 min when partially substituting 10 mol% of cupric ions by Mg^{2+} in $Cu(OH)_2$ (Fig. 5b). In Table 2, the pH of the supernatant sharply increases from $\approx$6 to $\approx$9 in the first 15 min after the immersion of $Cu_{0.9}Mg_{0.1}(OH)_2$ nanorods in water whereas pH remains around 6 for $Cu(OH)_2$. The small total concentration of DMPO-adducts in the suspension of $Cu_{0.9}Mg_{0.1}(OH)_2$ nanorods as well as its faster decay over time could partly be attributed to the decomposition of these adducts at the alkaline pH imposed by the partial dissolution of these nanorods in water (Table 2). Another factor could better explain the halving of the total concentration in DMPO-adducts after 7 min when partially substituting 10 mol% of cupric ions by Mg^{2+} in $Cu(OH)_2$. The production of free radicals is highly dependent on the surface chemistry of nanoparticles (*i.e.* the number of active sites). At the surface of nanorods, the high proportion of incomplete coordination spheres at the divalent cationic sites naturally promote adsorption of hydrogen peroxide molecules, the initial step allowing the formation of free oxygen radicals. However, between two cations, Cu^{2+} ions are the most active because they have a greater ability to be sub-coordinated to ligands (*i.e.* four- or five-fold coordinated) than Mg^{2+} ones and they can catalyse the generation of radicals from aqueous H_2O_2 through a Fenton-like redox cycling between Cu^{2+} and Cu^{+}/Cu^{3+} ions (eqn (1)–(5)). This explains why despite similar particle size, the $\log_{10}$ reduction in cell viability upon contact with $Mg(OH)_2$ nanoplatelets[37] is six order of magnitude lower than that measured with $Cu(OH)_2$ nanorods after 180 min. Thereby, we believe that the decrease in radicals amount produced when partially substituted Cu^{2+} by Mg^{2+} in $Cu(OH)_2$ nanorods also arises from the decrease in the number of sub-coordinated Cu^{2+} ions available for H_2O_2 adsorption at the surface.

EPR spin trapping study reveals that $Cu(OH)_2$ and $Cu_{0.9}Mg_{0.1}(OH)_2$ nanorods produce more than twice as many hydroxyl radical HO$^{\bullet}$ adducts ($^{\bullet}$DMPO-OH) as superoxide $O_2^{\bullet-}$ adducts ($^{\bullet}$DMPO-O_2^{-}/O_2H) in presence of hydrogen peroxide in the medium (7 : 3 ratio). Finkelstein *et al.*[63] evaluated that approximately 3% of the $^{\bullet}$DMPO-O_2H adducts formed during a spin-trapping experiment can directly decompose into $^{\bullet}$DMPO-OH adducts. Given the 7 : 3 ratio of adducts in our study, the partial dismutation of the $^{\bullet}$DMPO-O_2H adducts could only slightly increase the relative proportion of $^{\bullet}$DMPO-OH adducts detected in water suspensions. Thereby, the $^{\bullet}$DMPO-OH adducts result mainly from the trapping of free hydroxyl radicals intrinsically generated in large amount by nanorods in the water suspension. Because they are highly toxic to bacteria, hydroxyl radicals therefore play a key role in the exceptionally high bactericidal performances reported for both $Cu(OH)_2$ and $Cu_{0.9}Mg_{0.1}(OH)_2$ nanorods after 180 min (Table 1). The above EPR experiments also show that hydroxide peroxide is clearly involved in the bactericidal mechanism because its presence in the medium significantly increases the concentration of the free oxygen radicals produced by nanorods (Fig. 5).

4-Conclusion and perspective

Pure and Mg-substituted $Cu(OH)_2$ nanorods of about 15 nm in diameter and several hundred nanometers in length were successfully prepared by a simple co-precipitation at room temperature in mixed alkaline ($NaOH/Na_2CO_3$) medium. The partial substitution of cupric ions in $Cu(OH)_2$ by Mg^{2+}, even if it does not exceed 10 mol%, increases by a factor of 167 the solubility of the nanorods after 180 min in water (0.06 wt% and 10 wt% for $Cu(OH)_2$ and $Cu_{0.9}Mg_{0.1}(OH)_2$, respectively). Cupric ions are toxic in the free state above the minimal concentration (MIC) inhibiting the growth of bacteria or non-toxic, even in a very high concentration, when complexed with peptides of the culture medium. Because $Cu(OH)_2$ nanorods are practically insoluble in water whereas their lightly Mg-substituted counterparts are, sterile water was used as medium in the present study for determining the role played by released cupric ions in the bactericidal mechanism of $Cu(OH)_2$. Analyses by atomic emission spectroscopy confirm that, the mass concentration in cupric ions released from $Cu(OH)_2$ nanorods after 180 min in water is lower than minimal concentrations (MIC) required to inhibit the growth of *E. coli* and *S. aureus* ($\approx$69 and $\approx$34 times lower, respectively). Despite its insolubility in water, the entire initial inoculum of *E. coli* or *S. aureus* (100% reduction of one million CFU per mL or 6 $\log_{10}$ reduction) is killed after only 180 min on contact with the $Cu(OH)_2$ nanorods. The size reduction of the $Cu(OH)_2$ particles to about a hundred nanometers has significantly increased the moderate bactericidal activity of micron-sized aggregates of $Cu(OH)_2$ particles against *E. coli* reported so far (1 $\log_{10}$ after 480 min[16]). Partly soluble $Cu_{0.9}Mg_{0.1}(OH)_2$ nanorods also kill the entire initial inoculum of *E. coli* (6 $\log_{10}$ reduction) after 180 min, while only 0.01% of *S. aureus* is still alive (4 $\log_{10}$ or 99.99% reduction) after the same period of time. The pH increase induced by the dissolution of 10 wt% of the $Cu_{0.9}Mg_{0.1}(OH)_2$ nanorods in water causes the re-precipitation of 96.6 wt% of the released cupric ions in the form of $Cu(OH)_2$ particles. Thereby, the mass concentration in free cupric ions measured by AES in the water suspension of $Cu_{0.9}Mg_{0.1}(OH)_2$ nanorods, although it is higher than for $Cu(OH)_2$, also remains below the MIC. The toxicity of pure and Mg-substituted $Cu(OH)_2$ nanorods towards *E. coli* or *S. aureus* is therefore not linked to the very few free cupric ions present in water. Finally, EPR spin trapping study reveals how the nanorods kill bacteria in water: only the presence of hydrogen peroxide, a by-product of the normal metabolism of oxygen in aerobic bacteria, allows the $Cu_{1-x}Mg_x(OH)_2$ nanorods to produce lethal amount of free radicals, the majority of which are the highly toxic HO$^{\bullet}$. A precise knowledge of the toxicity of $Cu(OH)_2$ nanoparticles towards bacteria is now available.

Keller's group[64] observed that the commercial micron-sized aggregates of $Cu(OH)_2$ nanoparticles sprayed on spinach leaves, at agriculturally relevant doses to efficiently fight harmful microorganisms, significantly decreased a number of low-molecular-mass antioxidants, which are beneficial nutrients for humans. Although these authors postulated that reactive oxygen species could be the cause, our study provides the first experimental evidence that $Cu(OH)_2$ nano-pesticides do indeed produce free oxygen radicals. Collectively, the results reported herein demonstrates that in contrast, $Cu(OH)_2$ nanorods are better suited for water disinfection due to their extremely low solubility at neutral pH and a bactericidal activity towards *E. coli* and *S. aureus* meeting U.S. Food and Drug Administration standards.[5] In the future, $Cu(OH)_2$ nanorods could therefore have great application potential as a non-soluble antibacterial agent for recycling grey waters or decontaminating agricultural waters.

Author contributions

Batiste Clavier: investigation, formal analysis, visualization. Téo Baptiste: investigation. Antonii Zhadan: investigation. Amandine Guiet: investigation (transmission electron microscopy). Fabien Boucher: investigation (atomic emission spectroscopy). Vlasta Brezová: methodology, investigation, data curation (electron paramagnetic resonance). Christine Roques: methodology, investigation, data curation (bactericidal activity). Gwenaël Corbel: conceptualization, methodology, validation, formal analysis, data curation, writing – original draft, writing – review & editing, visualization, supervision, project administration, funding acquisition.

Conflicts of interest

There are no conflicts of interest to declare.

Acknowledgements

The French Ministry of Higher Education, Research and Innovation and Le Mans University are acknowledged for providing a doctoral grant to BC. The EPR study was financially supported by Scientific Grant Agency of the Ministry of Education, Science, Research and Sport of the Slovak Republic (VEGA Project 1/0064/21). VB thanks Ministry of Education, Science, Research and Sport of the Slovak Republic for funding within the scheme ''Excellent research teams''. CR thanks the Fonderephar for its technical support.

References

1 FAO, Food and Agriculture Organization of the United Nations-The post-2015 development agenda and sustainable development goals, http://www.fao.org/sustainable-development-goals/overview/fao-and-the-post-2015-development-agenda/water/en/, 2015, 1-28.
2 Y. Pachepsky, D. R. Shelton, J. E. T. McLain, J. Patel and R. E. Mandrell, in *Advances in Agronomy*, ed. D. L. Sparks, Academic Press, 2011, vol. 113, pp. 75–141.
3 O. A. Ijabadeniyi, L. K. Debusho, M. Vanderlinde and E. M. Buys, *J. Food Saf.*, 2011, **31**, 452–461.
4 E. F. S. Authority, *EFSA J.*, 2011, **9**, 2390.
5 United States Food and Drug Administration. Record of Decision for FSMA Final Rule on Produce Safety: Standards for the Growing, Harvesting, Packing, and Holding of Produce for Human Consumption, 2015, https://www.fda.gov/food/food-safety-modernization-act-fsma/fsma-final-rule-produce-safety.
6 R. Otterpohl, A. Albold and M. Oldenburg, *Water Sci. Technol.*, 1999, **39**, 153–160.
7 F. D. Lowy, *N. Engl. J. Med.*, 1998, **339**, 520–532.
8 P. K. Pandey, P. H. Kass, M. L. Soupir, S. Biswas and V. P. Singh, *AMB Express*, 2014, **4**, 51.
9 O. R. Al-Jayyousi, *Desalination*, 2003, **156**, 181–192.
10 N. Al-Jassim, M. I. Ansari, M. Harb and P.-Y. Hong, *Water Res.*, 2015, **73**, 277–290.
11 A. M. Dixon, D. Butler and A. Fewkes, *Water Environ. J.*, 1999, **13**, 322–326.
12 J. Ottoson and T. A. Stenström, *Water Res.*, 2003, **37**, 645–655.
13 A. Gross, D. Kaplan and K. Baker, *Ecol. Eng.*, 2007, **31**, 107–114.
14 T. A. Bellar, J. J. Lichtenberg and R. C. Kroner, *J. – Am. Water Works Assoc.*, 1974, **66**, 703–706.
15 World Health Organization (WHO), Trihalomethanes in drinking-water: background document for development of WHO guidelines for drinking-water quality, pp. 1–67. https://www.who.int/water_sanitation_health/dwq/chemicals/THM200605.pdf, 2005.
16 H. Karkhanechi, R. Takagi, Y. Ohmukai and H. Matsuyama, *Desalination*, 2013, **325**, 40–47.
17 M. Li, L. Zhu and D. Lin, *Environ. Sci. Technol.*, 2011, **45**, 1977–1983.
18 M. Hans, A. Erbe, S. Mathews, Y. Chen, M. Solioz and F. Mücklich, *Langmuir*, 2013, **29**, 16160–16166.
19 C. Gunawan, W. Y. Teoh, C. P. Marquis and R. Amal, *ACS Nano*, 2011, **5**, 7214–7225.
20 Z. H. Zhao, Y. Sakagami and T. Osaka, *Bull. Chem. Soc. Jpn.*, 1998, **71**, 939–945.
21 A. N. Pham, G. Xing, C. J. Miller and T. D. Waite, *J. Catal.*, 2013, **301**, 54–64.
22 T. T. M. Nguyen, H.-J. Park, J. Y. Kim, H.-E. Kim, H. Lee, J. Yoon and C. Lee, *Environ. Sci. Technol.*, 2013, **47**, 13661–13667.
23 *Handbook of Inorganic Chemicals*, ed. P. Patnaik, McGraw-Hill, USA, 2003.
24 *CRC Handbook of Chemistry and Physics 2008–2009: A Ready-Reference Book of Chemical and Physical Data*, ed. D. R. Lide, CRC Press, Boca Raton, Florida, USA, 2008.
25 M. J. Pack, W. Patalinghug and M. T. Weller, *J. Chem. Soc., Dalton Trans.*, 1996, **1**, 7–10.
26 D. N. Sathyanarayana, *Electronic Absorption Spectroscopy and Related Techniques*, Universities Press, 2001.

27 S. Stoll and A. Schweiger, *J. Magn. Reson.*, 2006, **178**, 42–55.
28 Y. Cudennec, A. Lecerf and Y. Gerault, *Eur. J. Solid State Inorg. Chem.*, 1995, **32**, 1013–1022.
29 Y. Cudennec, A. Riou, Y. Gérault and A. Lecerf, *C. R. Acad. Sci., Ser. IIc: Chim.*, 2000, **3**, 661–666.
30 J. R. Gunter and H. R. Oswald, *J. Appl. Crystallogr.*, 1970, **3**, 21–26.
31 Y. Liu, Y. Chu, M. Li, L. Li and L. Dong, *J. Mater. Chem.*, 2006, **16**, 192–198.
32 H. R. Oswald, A. Reller, H. W. Schmalle and E. Dubler, *Acta Crystallogr., Sect. C: Cryst. Struct. Commun.*, 1990, **46**, 2279–2284.
33 Y. Cudennec and A. Lecerf, *Solid State Sci.*, 2003, **5**, 1471–1474.
34 A. C. Cumming and A. Gemmell, *Proc. R. Soc. Edinburgh*, 1913, **32**, 4–11.
35 C. H. Yoder, E. Bushong, X. Liu, V. Weidner, P. McWilliams, K. Martin, J. Lorgunpai, J. Haller and R. W. Schaeffer, *Mineral. Mag.*, 2018, **74**, 433–440.
36 K. Nakamoto, *Infrared and Raman Spectra of Inorganic and Coordination Compounds*, John Wiley & Sons, Inc., 2008, ch. 2, pp. 149–354.
37 B. Clavier, T. Baptiste, F. Massuyeau, A. Jouanneaux, A. Guiet, F. Boucher, V. Fernandez, C. Roques and G. Corbel, *J. Mater. Chem. B*, 2020, **8**, 100–113.
38 Y. Fukuda and K. Tanabe, *Bull. Chem. Soc. Jpn.*, 1973, **46**, 1616–1619.
39 H. Tanaka and T. Sadamoto, *Thermochim. Acta*, 1982, **54**, 273–280.
40 R. S. Gordon and W. D. Kingery, *J. Am. Ceram. Soc.*, 1966, **49**, 654–660.
41 M. Fukuda and N. Koga, *J. Phys. Chem. C*, 2018, **122**, 12869–12879.
42 H. M. Rietveld, *Acta Crystallogr.*, 1967, **22**, 151–152.
43 J. Rodriguez Carvajal, *Phys. B*, 1993, **192**, 55–69.
44 J. I. Langford, *J. Appl. Crystallogr.*, 1978, **11**, 10–14.
45 T. H. de Keijser, J. I. Langford, E. J. Mittemeijer and A. B. P. Vogels, *J. Appl. Crystallogr.*, 1982, **15**, 308–314.
46 J. I. Langford, D. Louër, E. J. Sonneveld and J. W. Visser, *Powder Diffr.*, 1986, **1**, 211–221.
47 J. I. Langford, International Conference ''Accuracy in Powder Diffraction II'', May 26-29, 1992 at NIST, Gaithersburg, MD, USA, 1992, pp. 110–126.
48 A. Le Bail, H. Duroy and J. L. Fourquet, *Mater. Res. Bull.*, 1988, **23**, 447–452.
49 R. D. Shannon, *Acta Crystallogr.*, 1976, **A32**, 751–767.
50 L. Vegard, *Z. Phys.*, 1921, **5**, 17–26.
51 O. Akhavan, R. Azimirad, S. Safa and E. Hasani, *J. Mater. Chem.*, 2011, **21**, 9634–9640.
52 B. Clavier, T. Baptiste, Z. Barbieriková, T. Hajdu, A. Guiet, F. Boucher, V. Brezová, C. Roques and G. Corbel, *Mater. Sci. Eng., C*, 2021, **123**, 111997.
53 B. Chance, H. Sies and A. Boveris, *Physiol. Rev.*, 1979, **59**, 527–605.
54 M. Hricovíni, M. Mazúr, A. Sîrbu, O. Palamarciuc, V. B. Arion and V. Brezová, *Molecules*, 2018, **23**, 17.
55 D. Dvoranová, Z. Barbieriková, M. Mazúr, E. I. García-López, G. Marcì, K. Lušpai and V. Brezová, *J. Photochem. Photobiol., A*, 2019, **375**, 100–113.
56 C. Rota, D. P. Barr, M. V. Martin, F. P. Guengerich, A. Tomasi and R. P. Mason, *Biochem. J.*, 1997, **328**(Pt 2), 565–571.
57 D. B. Medinas, G. Cerchiaro, D. F. Trindade and O. Augusto, *IUBMB Life*, 2007, **59**, 255–262.
58 G. V. Buxton and A. J. Elliot, *Int. J. Radiat. Appl. Instrum., Part C*, 1986, **27**, 241–243.
59 E. Finkelstein, G. M. Rosen and E. J. Rauckman, *Arch. Biochem. Biophys.*, 1980, **200**, 1–16.
60 H. Zhang, J. Joseph, C. Felix and B. Kalyanaraman, *J. Biol. Chem.*, 2000, **275**, 14038–14045.
61 W. Dröge, *Physiol. Rev.*, 2002, **82**, 47–95.
62 C. D. Pericone, K. Overweg, P. W. M. Hermans and J. N. Weiser, *Infect. Immun.*, 2000, **68**, 3990.
63 E. Finkelstein, G. M. Rosen and E. J. Rauckman, *Mol. Pharmacol.*, 1982, **21**, 262.
64 L. Zhao, Y. Huang, A. S. Adeleye and A. A. Keller, *Environ. Sci. Technol.*, 2017, **51**, 10184–10194.